The Tropical Air-Sea Propagation Study (TAPS)

Andy Kulessa, Amalia Barrios, Jacques Claverie, Sally Garrett, Tracy Haack, Jorg Hacker, Hedley Hansen, Kate Horgan, Yvonick Hurtaud, C. Lemon, et al.

THE TROPICAL AIR–SEA PROPAGATION STUDY (TAPS)

A. S. Kulessa, A. Barrios, J. Claverie, S. Garrett, T. Haack, J. M. Hacker, H. J. Hansen, K. Horgan, Y. Hurtaud, C. Lemon, R. Marshall, J. McGregor, M. McMillan, C. Périard, V. Pourret, J. Price, L. T. Rogers, C. Short, M. Veasey, and V. R. Wiss

A field campaign designed to evaluate the ability to forecast radio wave propagation in a tropical coastal environment is discussed.

The Tropical Air–Sea Propagation Study (TAPS) was an international field campaign, combined with multimodel operational numerical weather prediction (NWP) forecasts, that took place off the northeastern coast of Australia, near the towns of Lucinda and Ingham. Its focus was on the collection of coordinated clear-air atmospheric and radio frequency (RF) datasets concurrent with near-real-time predictions of the environment from four mesoscale NWP systems. Measurements were made for the purpose of validating RF propagation forecasting methodologies and their constituent models: atmospheric surface-layer models, mesoscale NWP models, NWP surface-layer blending techniques, and radio wave tropospheric-propagation models. The initial interest is in applying such methodologies to maritime radar and communication operations as well as investigating the feasibility of novel beyond-the-line-of-sight communication networks. TAPS was not the first field campaign aimed at investigating radio wave propagation over the sea surface. Several notable campaigns, such as LORIENT 89 (Claverie and Hurtaud 1992), TOULON 90 (Claverie and Hurtaud 1992), Variability of Coastal Atmospheric

AFFILIATIONS: Kulessa—Cyber and Electronic Warfare Division, Defence Science and Technology Organisation, Edinburgh, and Airborne Research Australia, School of the Environment, Flinders University, Parafield Airport, South Australia, Australia; Barrios and Rogers—Atmospheric Propagation Branch, Space and Naval Warfare Systems Center Pacific, San Diego, California; Claverie—Centre de Recherche des Ecoles de Saint-Cyr Coetquidan (CREC), and Institut d'Électronique et de Télécommunications de Rennes, Guer, France; Garrett and Lemon—Defence Technology Agency, Auckland, New Zealand; Haack—Marine Meteorology Division, Naval Research Laboratory, Monterey, California; Hacker—Airborne Research Australia, School of the Environment, Flinders University, Parafield Airport, South Australia, Australia; Hansen—Cyber and Electronic Warfare Division, Defence Science and Technology Organisation, Edinburgh, South Australia, Australia; Horgan and Wiss—Dahlgren Division, Naval Surface Warfare Center, Dahlgren, Virginia; Hurtaud—Direction Générale de l'Armement Maîtrise de l'information, Rennes-Armées, France; Marshall—Mount Pleasant Meteorology, Woodford, Virginia; McGregor, McMillan, Price, Short, and Veasey—Met Office, Exeter, United Kingdom; Périard and Pourret—Météo-France, Toulouse, France
CORRESPONDING AUTHOR E-MAIL: Andy S. Kulessa, andy.kulessa@airborneresearch.com.au

The abstract for this article can be found in this issue, following the table of contents.

DOI:10.1175/BAMS-D-14-00284.1

In final form 21 June 2016

Refractivity (VOCAR; Paulus 1994), Rough Evaporation Duct (RED; Anderson et al. 2004), Validation Measurements for Propagation in the Infrared and Radar (VAMPIRA; Essen et al. 2006), Prediction of Electro-Magnetic Detection (PREDEM; Hurtaud et al. 2008), Microwave Propagation Measurement Experiment (MPME) at Wallops Island, Virginia (MPME WALLOPS2000; Stapleton et al. 2001), and New Zealand Sea Breeze Trial (Garrett et al. 2009), have been conducted at various locations around the world during the last 25 years. With the exception of RED, these campaigns took place in temperate waters, along the Atlantic coastlines of the United States and France, in the Mediterranean Sea, and in the Bay of Plenty, New Zealand. TAPS was, however, the first campaign in the Australian tropics that combined coordinated sea and land boundary layer measurements and weather prediction modeling with radio measurements, covering specific frequencies across the ultrahigh-frequency (UHF) to extremely high-frequency (EHF) bands.

The propagation of RF signals is strongly influenced by environmental factors. The coverage of ground-based transmissions over Earth's surface varies as environmental conditions change. Signal fading, multipath interference, and the ability of signals to propagate beyond the line of sight (sometimes referred to as "extended" propagation) are phenomena that commonly affect both communication and radar systems. These phenomena are influenced by refraction, absorption, scattering, and ducting (i.e., internal reflection) by the atmospheric medium as well as by reflection and diffraction by the surface. The variability of these phenomena in space and time make it challenging to predict propagation effects and even more so in coastal regions, where the marine environment differs greatly from that of land. The onset of atmospheric circulations and internal boundary layers combined with surface temperature gradients can lead to significant spatial and temporal changes in propagation.

The ability to forecast RF propagation coverage hours or days in advance would be an asset for optimizing RF services, such as predicting the performance of radar operations on board ships at sea. The significant variabilities in propagation effects are such that navies now employ RF signal coverage models that utilize meteorological observation or model inputs for sensor performance assessments. Recent progress in weather forecasting and propagation modeling combined with new in situ and remote sensing methods (Lowry et al. 2002; Rogers et al. 2000; Burk et al. 2003; Yardim 2007; Karimian et al. 2013; Xiaofeng and Sixun 2012) for the determination of either NWP model initial conditions or real-time refractive index data has made RF signal (e.g., radar coverage) forecasting to support marine radar operations at sea viable.

In general, RF coverage forecasting methodologies rely on two main steps: 1) forecasting the atmospheric refractive index and surface conditions and 2) calculating the signal coverage using appropriate radio wave propagation models that incorporate the information from step 1. Advancements in weather prediction suggest the use of mesoscale NWP models supplemented with atmospheric surface-layer models to forecast the refractive index (Atkinson and Zhu 2006; Haack et al. 2010; Wang et al. 2012). Signal propagation incorporating multipath interference lobing, diffraction, ducting, and various refraction effects can be modeled by the parabolic equation methods (Craig and Levy 1991; Barrios 1992; Dockery and Kuttler 1996; Levy 2000; Holm 2007), while other models are used to incorporate the effects of absorption and tropospheric scattering.

The TAPS campaign was primarily motivated by the need for improved RF coverage forecasting methodologies for ship radar systems, in particular for ships operating near coastlines, where the complexities of atmospheric flows and circulation patterns make accurate RF coverage prediction difficult. This study aims to provide a set of data to validate the end-to-end propagation forecasting process by enabling comparisons between observed and modeled meteorology and collocated observed and modeled RF coverage.

The TAPS campaign took place in the tropics, where certain ducting conditions known as evaporation ducts (discussed in the next section) prevail as a result of the warm sea surface. Past research of super-high-frequency (SHF) band (also known as microwave) propagation through the evaporation duct (Kulessa et al. 1998; Kerans et al. 2003) shows that the evaporation duct in these waters is capable of sustaining low-power, low-altitude microwave emissions over long distances. Woods et al. (2006, 2009) have considered the exploitation of the evaporation duct phenomenon as a means of developing a long-range, low-cost, low-power microwave communication system for the purpose of monitoring the conditions of the Great Barrier Reef. This novel concept has been demonstrated with the establishment of a 10-GHz experimental link between Davies Reef and the Australian Institute for Marine Science near Townsville, Queensland (Page et al. 2014). The TAPS datasets would facilitate a study of the viability of a novel microwave communications network extending for hundreds of kilometers, linking several communication nodes across the Great Barrier Reef.

In brief, this campaign facilitated a unique comparison of four different NWP systems with independent atmospheric measurements carried out by aircraft, radiosondes, kitesondes, and instrumented tower measurements throughout the boundary layer and especially the surface layer. RF data were collected at multiple frequencies within the UHF, SHF, and EHF bands, allowing propagation models to be assessed for measured and modeled refractive indices.

This paper outlines the TAPS campaign, describing the experiment design, the equipment and platforms used during the campaign, some preliminary results, and a synopsis of the more detailed analysis currently taking place. For readers primarily interested in radio science, this paper highlights the TAPS campaign as a major RF propagation study that investigates clear-air, beyond-the-line-of-sight propagation at frequencies in the UHF to EHF bands. For readers interested in boundary layer meteorology, this paper draws attention to the importance of surface data, surface-layer models, and NWP modeling for the forecasting of tropospheric radio wave propagation effects, and it highlights the extent of the turbulent flux data, bulk parameter data, and profile data collected during TAPS that would be especially useful for further research of the marine surface layer and also as a validation of mesoscale NWP models in tropical, littoral environments.

The next section describes tropospheric mechanisms that produce beyond-the-line-of-sight propagation and identifies some of the challenges facing NWP modeling as a means of forecasting the refractive index. The following section provides the field experiment design and measurement overview and then the initial results and preliminary findings of this work are presented. The paper concludes by summarizing ongoing and planned investigations that leverage the TAPS campaign measurements.

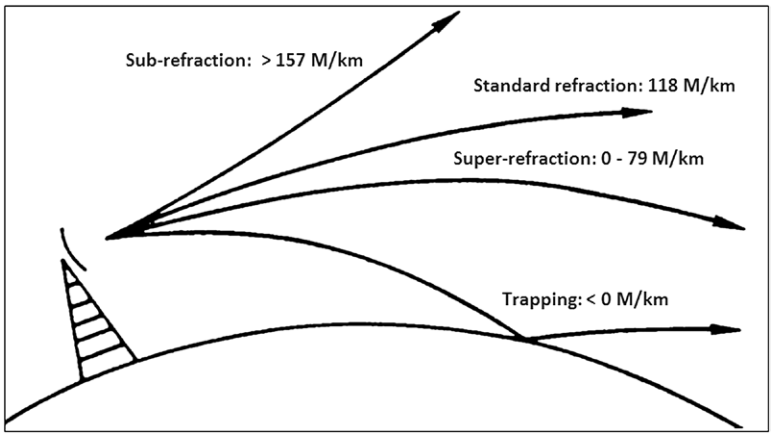

Fig. 1. Refraction of radio waves can be categorized as either subrefractive, standard, superrefractive, or trapping, depending on the vertical gradient of the modified refractivity (*M* units km^{-1}) of the atmosphere.

BACKGROUND. Clear-air tropospheric radio wave propagation depends strongly on the atmospheric refractive index, which is expressed in terms of atmospheric quantities by the Debye equation (Burrows 1968):

$$N = (n - 1) \times 10^6 = \frac{77.6}{T}\left(P + \frac{4810e}{T}\right), \quad (1)$$

where N is the refractivity (expressed in N units, which is a conversion of the refractive index n into a more suitable number); P is the atmospheric pressure (hPa); T is the atmospheric temperature (K); and e is the atmosphere's water vapor pressure (hPa). The vertical gradient of the refractivity and hence of the water vapor pressure, temperature, and pressure is critical for accurate radio wave propagation prediction. Therefore, an understanding of the dynamics and thermodynamics of the atmospheric boundary layer is vital for predicting radar performance, in addition to other services, such as wireless communications and broadcasting.

Several researchers have linked complex meteorological phenomena to significant changes in the propagation environment (Silveira and Massambani 1995; Brooks et al. 1999; Haack and Burk 2001; Thompson and Haack 2011) and many others have evaluated high-resolution NWP modeling of refractivity and ducting structures in the littoral (Atkinson and Zhu 2006; Haack et al. 2010; Marshall and Horgan 2011; Wang et al. 2012; Hurtaud and Claverie 2015). In coastal regions, significant temperature inversions and hydrolapses caused by the formation of internal boundary layers or sea-breeze circulations can produce superrefractive or ducting propagation conditions whereby a signal transmitted from Earth's surface, oriented parallel to the ground, can propagate well beyond the line of sight (Fig. 1). If the vertical lapses are strong enough, the associated change in the refractive index may cause some signals to be internally refracted within the layer and directed back toward the surface. Upon reflection from the surface, the process of atmospheric refraction and successive surface reflection is repeated and can lead

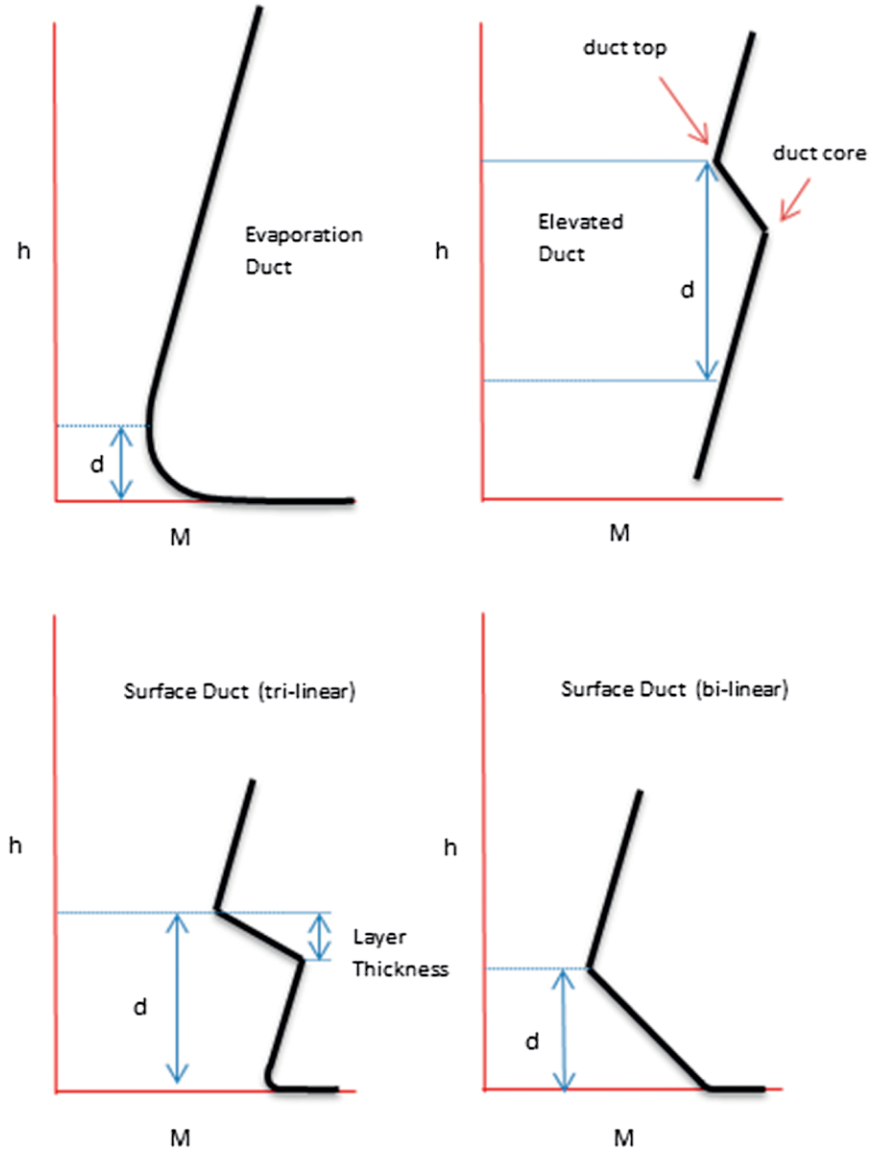

Fig. 2. Conceptual diagrams of the types of ducts observed during the TAPS campaign using schematic modified refractivity profiles, where *h* is height and *M* is modified refractivity: evaporation duct, elevated duct, and surface ducts with an evaporation duct. The letter *d* alongside the vertical arrows denotes the duct height (or thickness).

to propagation beyond the transmitter's horizon. In this sense, some of the radio wave energy is ducted, as in Fig. 1. A convenient way to show whether a duct is present is with the modified refractivity M (expressed in M units), defined from Eq. (1) as $M = N + 10^6(z/R_e)$, where z is the height above mean sea level and R_e is the Earth's radius in meters (Barrios 1992; Harish and Sachidananda 2007). This additional term accounts for the curvature of Earth such that a negative vertical gradient in M signifies a ducting layer.

Evaporation ducts are ubiquitous over the world's oceans as a result of evaporation processes close to the sea surface. A conceptual model of an evaporation duct is shown in Fig. 2. A characteristic feature is the very sharp decrease in modified refractivity, near the surface. There is then a gradual decrease of only several M units up to the duct height, at which point the value of M is at its minimum within the surface layer. The shape of the evaporation duct profile, the location of the evaporation duct height with respect to an RF transmitter height, and the frequency and orientation of the RF emissions are factors that determine how efficiently RF energy couples into the duct. When radio waves propagate inside an atmospheric duct, the duct may be thought of as a "leaky waveguide." For certain propagation modes, the leakage through the duct is small. Propagation theory shows that there is a critical "trapping" frequency that depends on the duct vertical gradient and the duct-layer thickness. Modes propagating below this critical frequency will mostly leak out of the duct, whereas modes above this critical frequency will be supported more efficiently by the duct. Past investigations of evaporation duct occurrence in the vicinity of the TAPS campaign show an average evaporation duct height of around 17 m, but with the possibility of duct heights in excess of 30 m (Kerans et al. 2000). An earlier but inconclusive study in the same region and season discusses how evaporation duct height scales with wind speed, showing duct heights of around 10 m in the presence of light winds [i.e., 3–4 m s^{-1}; Kulessa et al. (1997)]. These evaporation ducts are usually strong enough to support transmissions operating well within the SHF band and at higher-frequency bands.

The accurate forecasting of this surface-layer phenomenon can indeed be challenging for NWP models because of the simple fact that many vertical grid levels are required to adequately model the shape of the refractivity profiles. Improved representation of the near-surface structure can be obtained by blending NWP results with surface-layer model profiles. In thermally unstable conditions, and in the presence of a wind, the shape of the evaporation duct has been modeled using Monin–Obukhov similarity theory (Garratt 1994). The duct shape therefore depends on the surface-layer buoyancy, moisture, and momentum covariances and corresponding roughness lengths.

Ducts associated with gradients in the marine atmospheric boundary layer can occur in the presence of a hydrolapse, often accompanied by a temperature inversion, as in the case of a subsiding return flow within a sea-breeze circulation pattern. This action may cause elevated and surface ducts to form over the sea during the course of the diurnal cycle. Ducts formed in this manner are stronger than evaporation ducts and can also affect radio waves operating at very high-frequency bands (30–300 MHz) and UHF bands. The modified refractivity profiles tend to resemble either a bilinear or a trilinear curve, as shown in Fig. 2. Other processes such as the formation of nocturnal inversions, and the formation of stable internal boundary layers over the sea from advection processes, may result in ducting, producing bilinear and sometimes trilinear modified refractivity profiles, as shown in Fig. 2.

Often the vertical gradient of the modified refractivity dM/dh between the duct core and duct top is very steep, as shown in the example in Fig. 3. This diagram shows an elevated duct profile formed from a developed sea-breeze circulation, observed during the last day of the TAPS campaign. In this example, the modified refractivity M decreases by more than 30 units over a height gain of 60 m. Considering the pronounced impact that these modified refractivity lapses can have on propagation, and their variation in space and time, it may indeed prove challenging for current NWP models to accurately forecast these structures as closely spaced vertical grid levels and appropriate parameterization schemes would be required to accurately model the structure.

Ducting is not the only phenomenon that causes beyond-the-line-of-sight propagation. Atmospheric turbulence produces random fluctuations in temperature and humidity that may be sufficient to scatter radio wave signals well beyond the line of sight of the transmitting station. Although the scattering takes place in all directions, sufficient energy is directed back toward Earth to be detected by a suitable receiving system. This phenomenon is termed troposcatter. The extent of the turbulent and hence scattering atmospheric layer depends on various atmospheric processes made more complex in a coastal environment when two types of air masses interact.

FIELD EXPERIMENT DESIGN. *Site specification.* The TAPS area of operations was centered on Ingham, Queensland (18°39′S, 146°9′E), as shown in

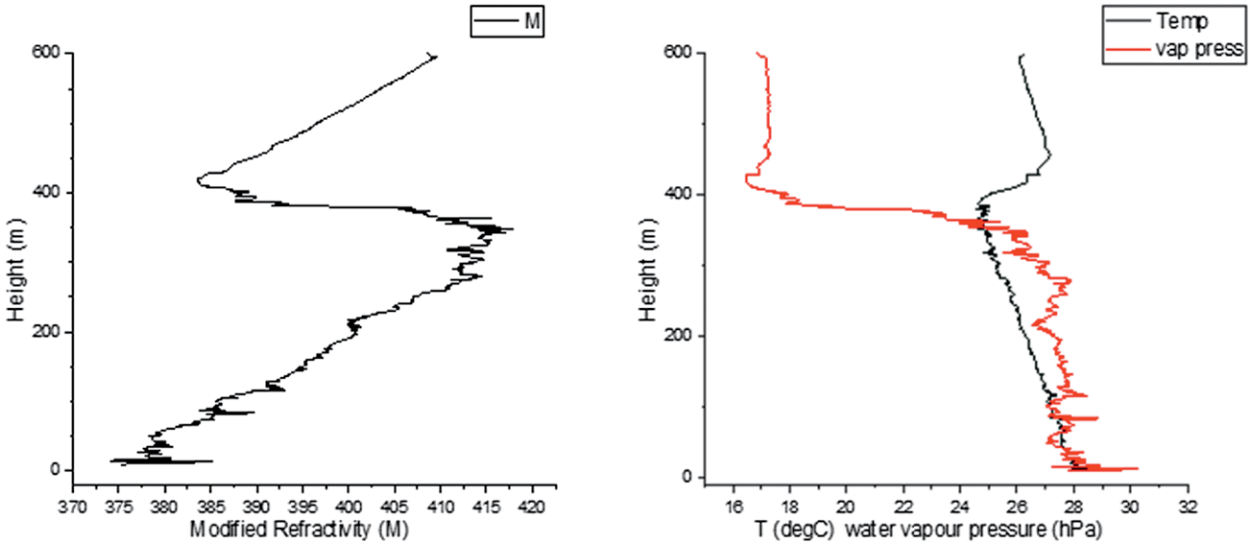

Fig. 3. (left) An example of an elevated duct profile measured by the aircraft during the late afternoon on 5 Dec 2013. The profile was measured between 35 and 40 km out to sea. (right) The duct formed by a sea-breeze circulation and the corresponding temperature inversion (black) and hydrolapse (red).

Fig. 4. The campaign took place over a 12-day period between 24 November and 5 December 2013, at the end of the spring season before the onset of tropical precipitation. The main advantages of carrying out the campaign in this area were the presence of a 6-km-long jetty providing a platform for surface measurements near the Lucinda coast over the Coral Sea, and the ability to transit an instrumented ship 80 km offshore from the Lucinda shore to the Great Barrier Reef without any topographic obstructions.

Instrumentation and measurements. Table 1 gives a summary of the platforms, equipment, and key measurements made during TAPS and Fig. 5 is a timeline of when each instrument was operating and collecting valid data. Ship and flight operations were conducted only during daylight hours, while other measurement systems ran continuously and are not detailed on this graph.

METEOROLOGICAL MEASUREMENTS. *LUCINDA JETTY.* The Defence Science and Technology Organisation (DSTO) deployed an instrumented tower at the end of the jetty to collect bulk sea temperatures, bulk meteorological parameters, and fast-response atmospheric data. Atmospheric temperature, humidity, and wind velocity were monitored for the purpose of determining turbulent flux (or covariance) quantities. The heights of the measurements varied roughly between 5 and 8 m above sea level, depending on the tides. Data from the fast-response Gill sonic anemometer and Li-Cor 7500A infrared gas analyzer (see Table 1) enabled the eddy-covariance method to be used in determining the scaling factors and roughness lengths necessary for the application of Monin–Obukhov similarity theory in deriving heat, moisture, and refractivity profiles for the surface layer (constant-flux layer) (Schotanus et al. 1983; Bradley 2003; Lee et al. 2008; Burba and Anderson 2012).

INGHAM AIRFIELD. The United Kingdom Meteorological Office (Met Office) measured temperature, humidity, winds, and pressure from a total of 49 radiosondes launched at Ingham Airfield. The Met Office also deployed a scanning Doppler lidar with a pulsed-laser system to measure the backscatter from aerosols and clouds in the atmosphere, while the Doppler shift of the returned signal gave the radial wind velocity. During TAPS, the lidar was configured to profile up to an altitude of 6 km, with a 30-m-height resolution. Wind-profiling scans were carried out every 15 min. Soil moisture and longwave and shortwave irradiance readings were collected at the same site, and, nearby, DSTO replicated their jetty flux instrumentation on a tower for measuring heat, moisture, and momentum fluxes over land.

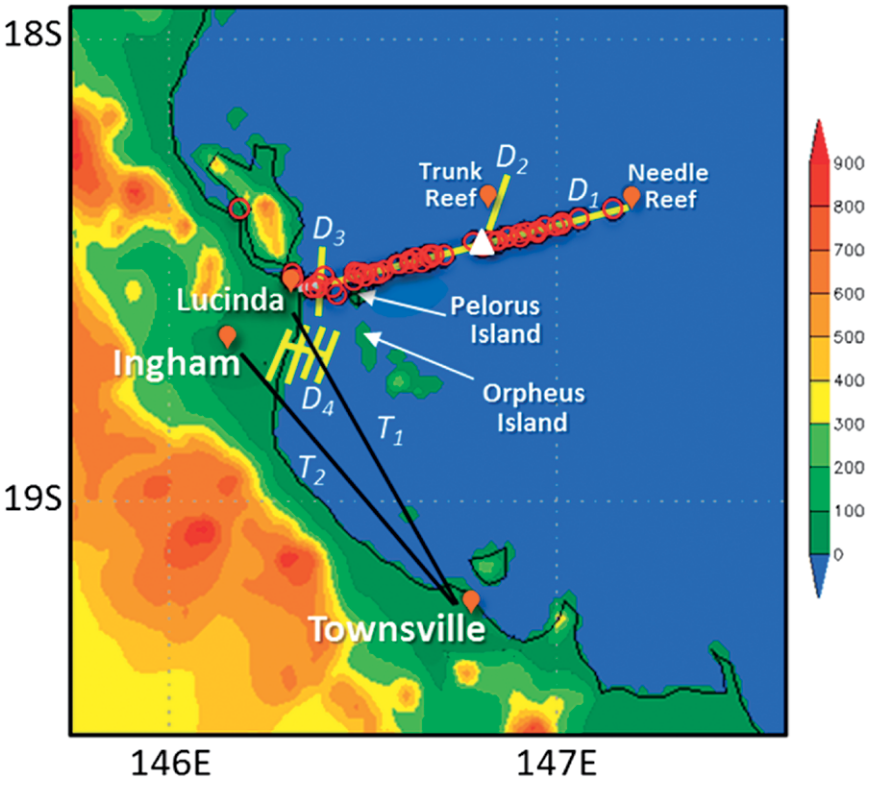

FIG. 4. Map of the TAPS field site, platform tracks, and identifying landmarks, with terrain height (color shaded; m). The yellow lines marked D are the primary ECO-Dimona flight tracks, and the black lines marked T are the troposcatter paths. The path D_1 denotes the primary track of the R/V *Cape Ferguson*, which also indicates the variable link propagation path, and the red circles show the locations of radiosondes.

RESEARCH VESSEL CAPE FERGUSON. The Research Vessel (R/V) *Cape Ferguson* operated between the township of Lucinda and Needle Reef (93 km offshore), during daylight hours, approximately between 2230 UTC

(0830 LT) and 0700 UTC (1700 LT). The locations of Lucinda, Needle Reef, and the track of the R/V are shown in Fig. 4. In addition to being the primary platform for collecting over-water meteorological measurements, the R/V accommodated eight RF receivers for measuring propagation path loss at four frequencies, as described in the section on meteorological measurements. The locations of the RF and meteorological instruments are shown in Fig. 6 on the aft of the vessel's three decks and mast. Vertical profiling of the marine atmospheric boundary layer was accomplished by the Naval Surface Warfare Center Dahlgren Division (NSWCDD), which launched a total of 65 radiosondes from the R/V. A controlled leak technique was employed to limit the altitude of the balloon flight to meet Australian airspace restrictions and to provide an upward and a downward sounding, giving a total of 130 profiles. The downward sounding typically descends several kilometers from the ship and is therefore uncontaminated by ship wake effects. This downward sounding was particularly important during TAPS, where because of sea states and winds the R/V was unable to provide optimal ship orientation to the wind to minimize ship wake effects. To obtain a range-dependent refractivity control dataset on each day, radiosondes were launched at specified distances from shore rather than at regular time intervals. Two surface meteorological systems were also employed on the R/V for continuous readings of near-surface parameters, and NSWCDD also used an infrared device for measuring sea surface temperature at the radiosonde launch times.

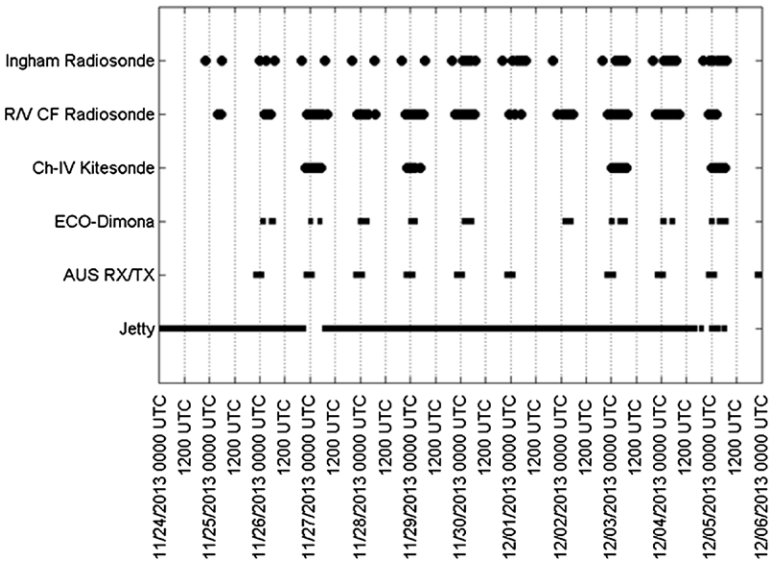

Fig. 5. Timeline of measurements collected for each platform.

Challenger IV/*kitesondes*. On 4 days of the campaign, the New Zealand Defence Technology Agency (DTA) operated a kitesonde at sea in the vicinity of Pelorus Island, measuring high-vertical-resolution atmospheric data near the sea surface. The kitesonde measurements aimed to provide data within the very turbulent surface layer for validation of modeled surface-layer profiling. The kitesonde consisted of a kite adapted to transport a radiosonde. The kite was connected to a motorized winch and flown off the aft deck of the vessel *Challenger IV*, a large catamaran owned and operated by James Cook University. As the vessel moved, the kite was released and slowly raised and lowered by the winch to obtain vertical profiles of air temperature, relative humidity, and pressure for heights near sea level up to about 120 m. Kitesonde profiles were collected on 27–28 November and on 3 and 5 December for a total of 102 profiles. The sampling rate of the system was 1 Hz and ascent and descent times ranged from 3 to 18 min, allowing between 200 and 300 data samples down to about 1.5 m above the sea surface.

Aircraft. The ECO-Dimona motor glider aircraft, a Diamond Aircraft HK36TTC (registration VH-OBS), owned and operated by Airborne Research Australia (see Fig. 7), flew on 8 of the 12 campaign days. The aircraft typically operated at cruising speeds between 50 and 100 knots (kt; 1 kt = 0.51 m s^{-1}) with an average flight time of around 6 h. The long wingspan (17.6 m) and slow cruising speed enabled low-altitude remote sensing and atmospheric profiling in the atmospheric surface layer and marine atmospheric boundary layer down to altitudes of 5 m above the water surface. The aircraft operating time varied between 7 and 8 h day^{-1} and daily flights were divided into a morning and an afternoon sortie with a 1-h intermission.

The instrumentation aboard the aircraft measured humidity, temperature, wind, and pressure profiles, as well as bulk parameters and turbulent flux quantities. Sea surface temperature measurements were recorded using infrared remote sensing equipment. A scanning lidar was used on the aircraft to determine wave height and sea state. A forward-looking time-tagged video camera recorded the (visual) atmospheric features during all flights. These sensors, summarized in Table 1, were housed in and

Table 1. A summary of platforms and sensors deployed for the TAPS field campaign. The locations and times of platform operations and data collected are detailed in Figs. 4 and 5.

Platform	Sensor	Organization
ECO-Dimona aircraft: Meteorological data	"Best" atmospheric turbulence (BAT) and Z Turbulence probes for 3D wind measurements	Airborne Research Australia and Flinders University, funded by NRL and the Met Office
	Fast ultrasensitive temperature sensor (FUST) temperature probe	
	Li-Cor 7500 open-path infrared gas analyzer (IRGA)	
	Meteolabor TP3 dewpoint mirror	
	Heimann KT15 IR surface temperature, dewpoint temperature, ambient pressure	
	Air angles, airspeed, 3D accelerations	
	OXTS RT4003 GPS/inertial measurement unit (IMU) system: position, altitude, attitude, time, 3D acceleration	
	Riegl Q240 scanning lidar	
	Forward-looking time-tagged video camera	
Lucinda jetty instrumented tower: Meteorological data	Gill sonic anemometer	DSTO
	Li-Cor 7500A IRGA	
	Vaisala HMP 155 slow-response temperature and humidity	
	OTT radar level sensor (RLS) radar-height sensor	
	Campbell Scientific 108 sea surface temperature sensor	
	Vaisala PTB330	
Lucinda shore		
RF data (tower and transmitters)	Four 35-GHz transmitters	Custom build by DSTO
	9-, 17-, and 94-GHz transmitters	
RF data (transmitter)	9.4-GHz transmitter	DTA
R/V *Cape Ferguson*		Australian Institute of Marine Science (AIMS), funded by DSTO
Meteorological data	Weatherpak2000 surface meteorological station	NSWCDD
RF data (receivers)	Vaisala RS-92 radiosondes, Cole Palmer 39800 IR SST	
	TeKI 9.4-GHZ receiver	DTA
	35-GHz band multi-input, multioutput (MIMO) distributed antenna receiving system	DSTO
	9-, 17-, 35-, and 94-GHz receivers	
Challenger IV: Meteorological data (kitesondes)	Motorized winch, fishing kite, Vaisala RS-92 radiosonde	James Cook University, funded by DSTO
		DTA
Ingham Airfield: Meteorological data	Vaisala RS-92 radiosondes, soil moisture content from an ML2 Delta-T ThetaProbe, downwelling longwave and shortwave irradiances from Kipp and Zonen CMP21 and CGR4 sensors, scanning Doppler lidar by Halo Photonics	Met Office
	Instrumented tower resembling the Lucinda jetty tower	DSTO
Digital TV signal of opportunity (DTV) SigOp RF data		Space and Naval Warfare Systems Command (SPAWAR)
Lucinda	Yagi 14-dB*i* gain antenna, HP 8594E spectrum analyzer	
Ingham	Shakespeare 4265BB antenna, Tektronix 3408A spectrum analyzer	

around specially designed pods that fit under both aircraft wings.

Aircraft operations encompassed four mission types and two primary flight patterns: straight and level transects at various heights (typically 10, 20, 40, 80, and 160 m above sea level) and sawtooth soundings throughout the surface layer and marine atmospheric boundary layer, sometimes descending to 5 m above sea level. The aircraft missions were categorized as follows:

i) Jetty tower (D_3 in Fig. 4) (26, 27, and 30 November and 2 December): For the purpose of aircraft calibration and instrument validation, transects were flown past the jetty tower, enabling aircraft-based momentum, heat, and moisture fluxes to be compared with tower flux measurements. Sawtooth soundings enabled the comparison of aircraft profiles with Monin–Obukhov similarity theory (Monin and Obukhov 1954; Garratt 1994) profiles derived from the jetty data.
ii) R/V propagation path (D_1 in Fig. 4) (26, 29, and 30 November and 2–5 December): Vertical profiles as well as flux and bulk parameter measurements were made using both sawtooth and transect runs along the R/V's track. The sawtooth runs captured surface-layer details down to heights as low as 5 m above the sea surface and interesting inversion features at the top of the marine atmospheric boundary layer. Sawtooth patterns were also flown in the vicinity of the kitesonde operations for comparison with those data.
iii) Trunk Reef (D_2 in Fig. 4) (29 November and 4 December): The aircraft performed stacked transects over and alongside Trunk Reef for bulk parameter and flux measurements. Daytime sea surface temperature readings inside coral lagoons may be sufficiently higher than their surroundings to enhance convective processes, affecting the shape of the evaporation duct. The details of the refractivity within lagoons are important for understanding sensor performance for systems exploiting the evaporation duct.
iv) Boundary layer land–sea transition (D_4 in Fig. 4) (5 December): Transect flux runs within the coastal boundary layer were conducted parallel to the coastline over the sea and over land. Data from this exercise are being used to investigate variations in gradient structures across the coastline and determine their impact on low-elevation terrestrial propagation and radar performance.

RF measurements. There were three RF propagation datasets collected during TAPS. Two utilized the Lucinda–R/V variable-range link, including DSTO's microwave–millimeter wave measurement system and DTA's Te Kupenga Irirangi Radar Tracking System (TeKI), an autonomous electronic surveillance system that detects and identifies radars. A third experiment by Space and Naval Warfare Systems Center Pacific (SSC-Pacific) investigated troposcatter of UHF television signals between Townsville and Lucinda or Ingham.

Variable-range RF link. RF signal-level measurements were carried out over a variable-range path between the coast of Lucinda and the R/V, which tracked each day toward Needle Reef (see Fig. 4). DSTO provided a height-distributed multiband transmit–receive network of RF links for investigating propagation in the SHF and EHF frequency bands. Each transmit element of the network, located on the shore at Lucinda, was provided with a characteristic wave signal (continuous-wave-, frequency-, and phase-modulated waveforms) that was modulated onto a specific RF carrier. Height-distributed receiver elements mounted on board the R/V, each tuned to a specific RF, then provided the characteristic down-converted signal outputs. The 9-, 17-, and 94-GHz frequencies were transmitted at 4.95 m above the ground from a tower on the Lucinda shore. Receivers for these frequencies were mounted at 8.7 m above sea level on board the R/V. The 35-GHz signals were transmitted at four heights above ground level (1.45, 3.45, 4.95, and 6.45 m) and four receive antennas were mounted (3.4, 5.7, 8.7, and 11.3 m above sea level) on the decks and mast of the R/V. The receiver network therefore comprised seven elements. This setup allowed for multiple geometries and thus provided a more comprehensive characterization of the propagation environment in the vicinity of the evaporation duct.

In addition to the DSTO RF system, DTA operated a radar unit at 9.4 GHz, erected 1.5 m above sea level in the township of Lucinda, near the coastline. Two TeKI receivers were mounted on the top deck of the R/V at a height of 10 m above sea level and operated at a frequency of 9.4 ± 0.1 GHz with horizontal polarization and a scan rate of 3° s^{-1}. It therefore received transmissions from multiple sources besides the Lucinda radar unit, including shipboard radars operating outside the Great Barrier Reef in the shipping lanes.

Signals of opportunity. Remote sensing of propagation loss via signals of opportunity (e.g., GPS, ship navigation systems, and TV and radio stations) is a reemerging area of research as a form of estimating refractivity information. Early research was conducted using

Fig. 6. Instrumentation aboard the R/V *Cape Ferguson* during TAPS. See Table 1 for details.

shipboard clutter maps to estimate propagation and to invert the propagation loss pattern to candidate refractive profiles (Rogers 1996; Lowry et al. 2002). Remote sensing has also been used for the extraction of the refractive index structure function parameter c_n^2 (Nilsson and Haas 2010) and has implications for understanding troposcatter effects on radio wave transmissions. Passive monitoring of digital television stations is another signal of opportunity and potential source of information on the propagation medium. During TAPS, signal-of-opportunity RF data were collected by two different means:

Ship navigation systems. The TeKI receiver system was able to de-interleave transmission characteristics from the fixed radar emitter at Lucinda and other transmitters operating within the system's reception bandwidth. In this way, the TeKI was also able to capture signals of opportunity from other emitters, typically operating along the shipping route just inshore of the Great Barrier Reef. The locations of these emitters were determined using the Automatic Identification System, which is compulsory in this area of the Great Barrier Reef. The power of the radar was confirmed at the closest point of approach to the system where atmospheric attenuation was minimal. This approach enabled atmospheric attenuation of emitters to be quantified over long one-way paths in excess of 120 km.

Digital television signals. RF receiving systems were located in Ingham and Lucinda to monitor digital television emissions from transmitters in Townsville (Fig. 4). These UHF receivers were used to study troposcatter by passively monitoring signals transmitted over 100 km away. During the TAPS campaign, monitoring of the 599.5-MHz television station in Townsville by a narrow bandwidth improved the signal-to-noise ratio at the receiver. The monitoring antenna in Ingham was oriented at 45° from vertical (so as to receive both horizontally and vertically polarized signals).

NWP modeling. During the campaign, three countries ran their operational mesoscale model forecasting systems in near–real time to support TAPS operations and daily mission planning and to produce predictions of environmental effects on RF propagation. These models included the U.S. Navy's Coupled Ocean–Atmosphere Mesoscale Prediction System (COAMPS[1]; Hodur 1997) run by the Naval Research Laboratory–Monterey (NRL-MRY), the United Kingdom's Unified Model (MetUM; Brown et al. 2012) run by the Met Office, and the French Applications de la Recherche à l'Opérationnel à Méso-Echelle (AROME; Seity et al. 2011) run by Météo-France. Australia and New Zealand share operational forecasts from the Regional Atmospheric Modeling System (RAMS; Pielke et al. 1992), which were archived and made available for postexperiment analysis together with the other models. Table 2 contains a summary of the model configurations and forecast designs employed for the TAPS campaign. The TAPS forecasts, and subsequent hindcasts from the NWP systems, are being used in a follow-on model intercomparison study to evaluate operational capabilities and improvements to environmental predictions in support of RF propagation modeling.

During the campaign, the models were run in a manner consistent with each country's real-time

[1] COAMPS is a registered trademark of the Naval Research Laboratory.

operational constraints, and thus attempts were not made to match model configurations. Three of the models posted specialized weather products to web servers that were used during on-site briefs and in asset allocation decisions. While COAMPS uses an "incremental update," the AROME and MetUM were run by dynamical downscaling global model forecasts to a single nest. Météo-France ran 48-h forecasts that were optimally available for the morning briefs because of their 0600 and 1800 UTC initializations. The forecasts were coupled with a French surface-layer model, Profils d'Indices de Réfraction en Atmosphère Marine (PIRAM; Claverie et al. 1998), to produce evaporation duct profiles. The Met Office provided forecasts out to 72 h at both 70 and 140 vertical-level distributions, which were used for visibility, precipitation, and longer-term planning. Each country's global model, which provides synoptic information to the mesoscale model through the outer nest's lateral boundary, took advantage of the four daily radiosonde observations (two additional launches per day) made possible by France's World Meteorological Organization (WMO) station located at New Caledonia, ~2000 km east of Lucinda.

Fig. 7. The ECO-Dimona, flying past the Lucinda jetty during TAPS. Two air turbulence probes are seen mounted underneath the aircraft wing. (inset) The ECO-Dimona at Ingham Airfield. The instrument pods under the wings are clearly visible.

INITIAL ANALYSIS AND RESULTS. A brief description of the weather patterns affecting the TAPS region facilitates the presentation of the initial results. Weather patterns near the jetty were fairly benign with light prevailing winds directed mainly onshore, high sea surface temperatures of approximately 29°C at the Lucinda jetty, and very moist conditions averaging 18 g kg^{-1} for the first 7 days of the experiment. Throughout most of the TAPS campaign there was evidence for sea–land breeze circulations. Two large-scale transitions to higher pressure resulted in sustained easterly winds and increased speeds prevented the formation of sea–land breezes for short periods. The high pressure caused downwelling air to create a capping inversion above the marine atmospheric boundary layer, but its height was generally well above 500 m, resulting in elevated ducts that did not have a significant impact on the propagation of TAPS surface sensors. Surface ducting did occur early in the experiment and briefly near the jetty on a few other occasions associated with local mesoscale flows. However, radio wave energy from surface transmitters was more likely influenced by variations in the evaporation duct. With an increase in wind speed on 1–2 December, the evaporation duct height approached 17 m but otherwise was found to be between 8 and 12 m in height, based on the NWP models (Fig. 8). The TAPS transmitters therefore usually resided within the evaporation duct, while at times some of the receivers aboard the R/V would have been above it.

NWP analysis. For an 86-h window from 2 to 5 December, a time series of the bulk jetty data is shown overlaid with each NWP model's hourly forecast from the nearest model grid point (Fig. 8), along with the computed modified refractivity (at a height of 10 m) and evaporation duct height. The shape and height of the evaporation duct was diagnosed by first computing high-resolution (1-m vertical spacing) Monin–Obukhov surface-layer profiles of temperature and specific humidity. These were obtained using the hourly forecasts of 10-m temperature and specific humidity, sea level pressure, and sea surface temperature. Computation of the surface-layer refractivity profile followed Eq. (1) and included the Earth curvature term to produce modified refractivity.

Table 2. NWP model configurations and forecast designs employed for TAPS study. BC= boundary conditions.

Model (organization)	Resolution: vertical (V) and horizontal (H)	First guess and inner nest	BC update: outer nest (O) and inner nest (I)	Sea surface temperature (SST) update	Data assimilation
COAMPS (NRL-MRY)	V: 60 sigma–z; number of NWP model levels up to 1 km (AVG_{1km}) =19 levels, ~54 m H: four nests (36, 12, 4, 1.67 km)	Two times daily (0000 and 1200 UTC) from each nest's pre-12-h forecast	O: 6-hourly from Navy Global Environmental Model (NAVGEM) I: every time step from 4-km nest	Navy Coupled Ocean Data Assimilation (NCODA) multivariant optimal interpolation (MVOI) analysis at grid resolution	Four-dimensional variational data assimilation (4DVAR) in NAVGEM, 6-hourly incremental update (IU) three-dimensional variational data assimilation (3DVAR) on each nest
MetUM (Met Office)	V: 70 hybrid heights; AVG_{1km} =16 levels, ~66 m H: one nest (4 km)	Two times daily (0000 and 1200 UTC); Dynamic downscaling from global-scale MetUM (Global-MetUM) pre-12-h forecast	O: 3-hourly from Global-MetUM	Daily (0000 UTC) from Operational Sea Surface Temperature and Sea Ice Analysis (OSTIA) at ~5-km resolution	4DVAR in Global-MetUM
AROME (Météo-France)	V: 60 sigma–p; AVG_{1km} =15 levels, ~65 m H: one nest (2.5 km)	Two times daily (0600 and 1800 UTC); Dynamic downscaling from European Centre for Medium-Range Weather Forecasts (ECMWF) pre-6-h forecast	O: 1-hourly from ECMWF	Daily (0000 UTC) from OSTIA at ~5-km resolution	4DVAR in ECMWF
RAMS (Royal Australian Navy)	V: 34 sigma–z; AVG_{1km} = 14 levels, ~77 m H: three nests: (12, 4, 1.67 km)	Two times daily (0000 and 1200 UTC); Dynamic downscaling from Australian Community Climate and Earth-System Simulator (ACCESS) pre-12-h forecast	O: 4-hourly from ACCESS I: 4-hourly from ACCESS	Daily (0000 UTC) from Sparse Hydrodynamic Ocean Code (SHOC) at ~5-km resolution	4DVAR in ACCESS

The height of the minimum in modified refractivity yielded the evaporation duct height estimates determined by each forecast model shown in Fig. 8.

The last 4 days of TAPS featured easterly winds that gradually decreased below 5 m s^{-1} until the passage of a weak front on 4 December. This transition caused the winds to rotate to a northerly direction, along with a sharp decrease in the nighttime air temperature and increase in moisture due to clear-sky conditions. The synoptic evolution is captured by all four models, although COAMPS's timing is delayed by about 3 h and RAMS performed poorly with its coarser vertical and horizontal resolutions relative to the three other mesoscale systems. The trend in evaporation duct height closely follows that of wind speed, with weaker wind speeds producing weaker surface fluxes and resulting in a smaller vertical gradient and hence lower evaporation duct heights. Alternatively, the modified refractivity is more sensitive to changes in specific humidity, revealing an abrupt increase in modified refractivity with the air-mass transition that brought in higher moisture amounts on 4 December. During this period of weak synoptic forcing there is evidence of a sea–land breeze influence on ducting and a diurnal signature in near-surface refractivity. Gradual nighttime cooling and moistening of the land created a land breeze that advected over the warm seas, resulting in a decrease in the evaporation duct height by half its daytime value and an increase in refractivity by about 15 M units.

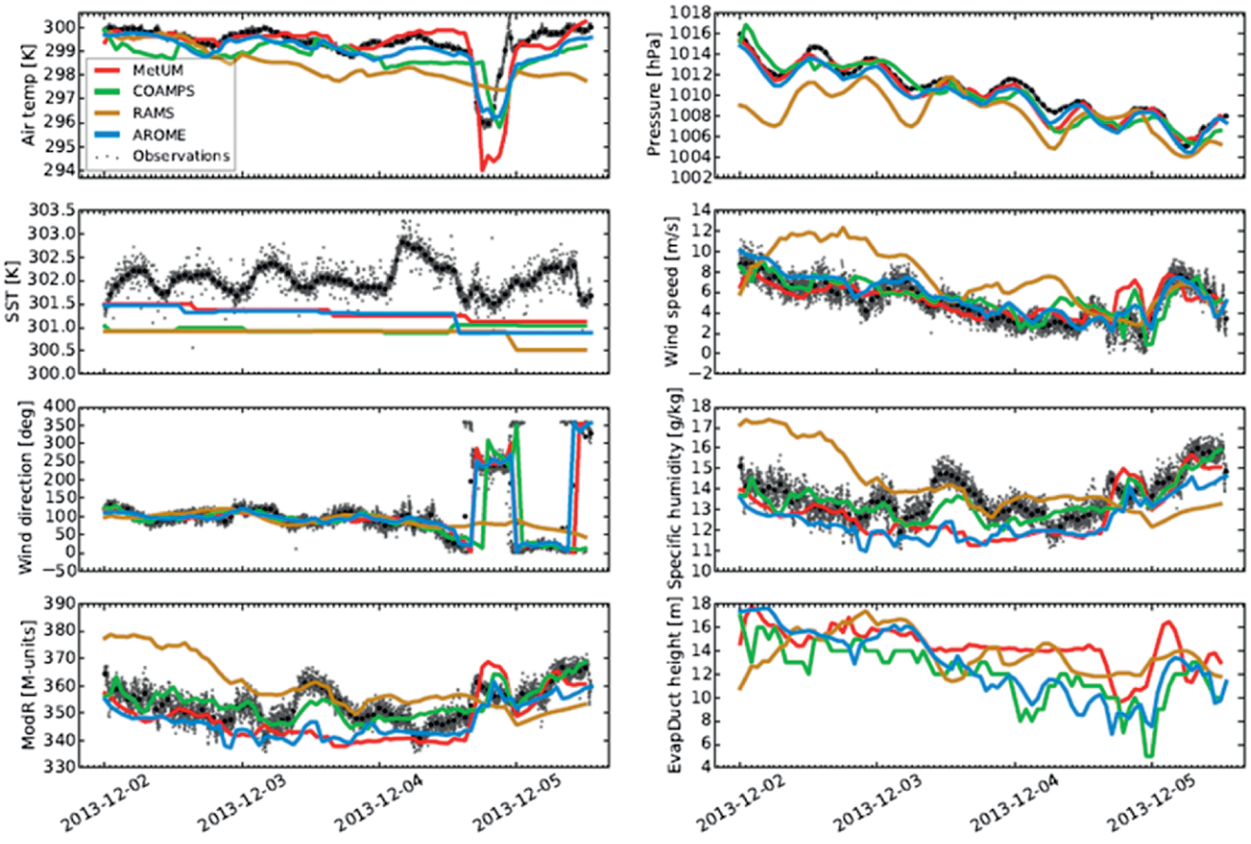

Fig. 8. Near-surface meteorological parameters measured at the jetty (gray dots) and collocated hourly forecasts at ~10-m level from each of the four mesoscale models: MetUM (4-km grid; red), COAMPS (1.67-km grid; green), AROME (2.5-km grid; blue), and RAMS (12-km grid; yellow) from 0000 UTC 2 Dec to 0000 UTC 6 Dec 2013.

Table 3 summarizes for each model the measured parameter and forecast performance statistics over the 86-h period. For a given parameter, the forecast is considered acceptable if the root-mean-square error is less than its variability, represented by the standard deviation. With the exception of RAMS, all models fall into this category for the near-surface jetty observations of wind speed and air pressure. Differences between each model are more apparent in air temperature and specific humidity. RAMS exhibits a significant cool bias of over 1 K, with COAMPS also showing a cool bias but to a much lesser extent. COAMPS, however, returns the smallest bias and root-mean-square error in specific humidity compared to the other models. Both MetUM and AROME have a dry bias that causes a higher error in specific humidity relative to the standard deviation. This discrepancy in the model moisture prediction affects the modified refractivity statistics, with AROME producing a root-mean-square error in modified refractivity that is slightly larger than its standard deviation.

The surface-layer models that are used to model the evaporation duct are based on Monin–Obukhov similarity theory. The scaling parameters (covariances) and roughness lengths are parameterized by an iterative scheme dependent on the bulk parameters of temperature, humidity, and wind speed at a given height and at the surface. The models show some consistency in evaporation duct height trends over the 4 days with a decrease to around 8 m near 2000 UTC 4 December (0600 LT 5 December) before rebounding to heights near 14 m during the day (Fig. 8). However, the models yield significant differences in evaporation duct height values of about 6 m during the daylight hours on 4 December. The RAMS model bulk parameters are consistently different from the other three models and so there is little surprise that the evaporation duct height estimates are different from AROME and COAMPS. What is surprising however is the yet-unexplained result as to why the MetUM evaporation duct height follows the trend of RAMS after 3 December. A detailed analysis of the surface-layer measurements and modeling techniques is currently in progress.

The vertical structure of the marine atmospheric boundary layer, 50 km from Lucinda, in the vicinity of Trunk Reef, at 0100 UTC 5 December, is shown

Table 3. Near-surface statistics at Lucinda jetty between 0000 UTC 3 Dec and 0000 UTC 6 Dec computed from bulk measurements and each model forecast. The first and second numbers outside the parentheses (separated by a slash) are the mean and standard deviation, respectively. The first and second numbers inside the parentheses (separated by a slash) are the bias (model minus observation) and rmse, respectively.

	COAMPS	MetUM	AROME	RAMS
Air temperature (K)	298.7/0.6	299.2/1.2	299.0/0.8	298.1/0.8
	(−0.6/0.9)	(−0.1/0.7)	(−0.4/0.6)	(−1.3/1.5)
Pressure (hPa)	1010.1/2.9	1010.1/2.5	1009.8/2.4	1003.3/2.8
	(−0.4/1.0)	(−0.3/0.6)	(−0.7/0.7)	(−7.2/7.3)
Wind speed (m s^{-1})	5.6/1.7	5.3/1.3	5.7/1.9	7.8/2.4
	(0.5/1.3)	(0.2/1.2)	(0.6/1.0)	(2.7/3.5)
Wind direction (°)	93.1/62.5	101.1/70.0	109.0/75.8	92.5/16.6
	(−18.4/81.1)	(−6.5/37.3)	(−1.6/34.3)	(−18.4/73.4)
Specific humidity (g kg^{-1})	13.3/0.9	12.8/1.2	12.4/0.9	14.2/1.6
	(−0.2/0.7)	(−0.8/1.1)	(−1.2/1.3)	(0.6/2.0)
Modified refractivity (*M* units)	353.6/5.7	348.2/8.7	347.0/6.1	358.4/10.0
	(0.4/4.6)	(−5.2/7.9)	(−6.4/7.9)	(4.9/12.8)
Evaporation duct height (m)	12.1/2.3	14.3/1.7	12.8/2.8	13.9/1.6
Count	86	86	86	86

in Fig. 9. Observations from the R/V radiosonde are overlaid with collocated NWP model profiles from the nearest grid point, even though grid spacings and forecast times for the NWP models are quite different. Horizontal grid spacings range from 1.67 to 12 km, while forecasts range from 1 to 25 h, as explained in Fig. 9. All of the models forecast a weaker-than-observed hydrolapse, primarily due to a weaker gradient and higher moisture aloft. Except for MetUM, the potential temperatures in the marine atmospheric boundary layer are slightly colder than the radiosonde measurements and the inversion is too smooth. Other than RAMS, the modeled modified refractivity profiles show an elevated duct with a weaker dM/dh gradient between the duct core and duct top. This is partly due to the vertical grid spacing being too coarse at about 100-m thickness near the height of the inversion and the type of turbulent mixing scheme used within each model. Although there is closer agreement between COAMPS and AROME, these profiles underestimate the inversion height whereas MetUM overestimates it—the difference between the modeled inversion heights being about 250 m. If these NWP model refractivity profiles were used in conjunction with the same propagation model to predict RF coverage of transmissions from a fixed height, coupling into the elevated duct, the results would be quite different because the refractivity profiles are different.

These preliminary results show discrepancies in the ability of the NWP models to predict surface-layer values as well as modified refractivity gradients associated with elevated ducts, indicating that improvements to the modeling are desirable. One of the key aims of TAPS is to facilitate NWP research that improves the characterization of temperature inversions, hydrolapses, and duct structure. Research currently being carried out as a result of TAPS includes the optimization of horizontal and vertical NWP resolution, adaptation of parameterization schemes for use in tropical environments, and investigations into novel data assimilation methods.

Comparing jetty and aircraft profiles. A comparison of the refractivity profiles derived from the jetty tower flux values and aircraft during different sorties is presented in Fig. 10. While the aircraft refractivity data were derived from explicit measurements of pressure, temperature, and humidity, profiles from the jetty flux measurements were derived using Monin–Obukhov similarity theory, which applies to the surface layer in situations where turbulence dominates, and is most reliable for the unstable atmosphere, as was the case throughout most of the TAPS period.

To briefly outline the approach used in the analysis (Kulessa and Hacker 2010), flux–gradient relationships for wind, virtual potential temperature, and specific humidity resulting from first-order closure are given as

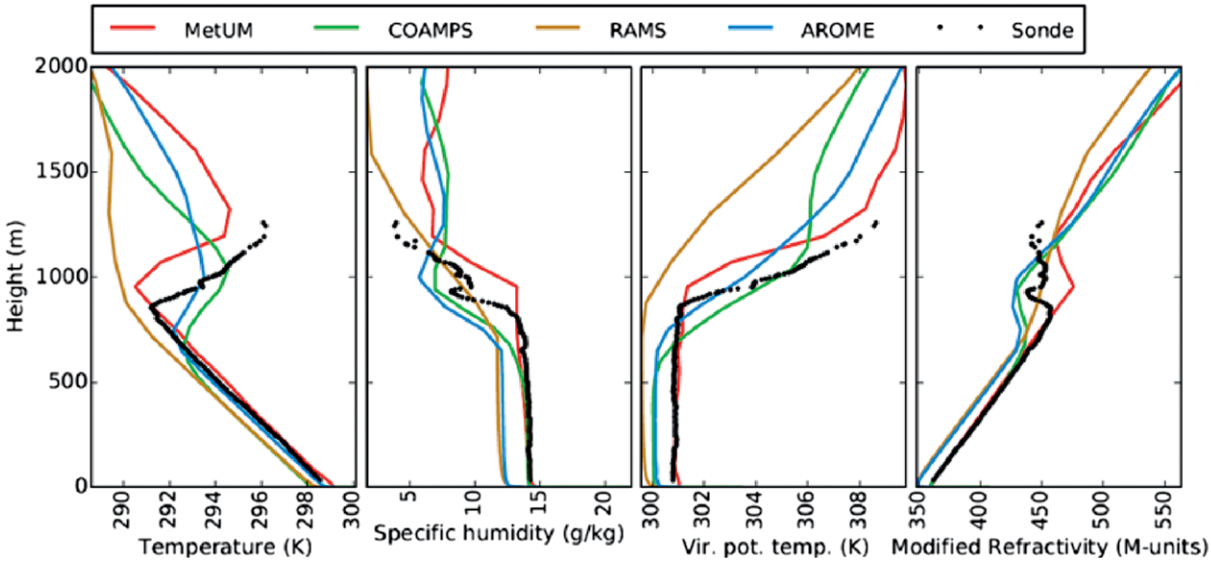

Fig. 9. Vertical profiles of temperature (K), specific humidity (g kg^{-1}), virtual potential temperature (K), and modified refractivity (*M* units) at 0100 UTC 5 Dec 2013 from a radiosonde (black dots) launched off of the R/V, overlaid with forecasts from each of the four NWP models: MetUM (4-km grid, 1-h forecast; red), COAMPS (1.67-km grid, 1-h forecast; green), AROME (2.5-km grid, 7-h forecast; blue), and RAMS (12-km grid, 25-h forecast; yellow).

$$\frac{\partial \overline{u_h}}{\partial z} = \frac{\left(\overline{u'w'}^2 + \overline{\upsilon'w'}^2\right)^{1/4}}{kz}\phi_m$$
$$\frac{\partial \overline{\theta_\upsilon}}{\partial z} = -\frac{\overline{\theta_\upsilon' w'}}{kz\left(\overline{u'w'}^2 + \overline{\upsilon'w'}^2\right)^{1/4}}\phi_H \qquad (2)$$
$$\frac{\partial \overline{q}}{\partial z} = -\frac{\overline{q'w'}}{kz\left(\overline{u'w'}^2 + \overline{\upsilon'w'}^2\right)^{1/4}}\phi_M .$$

The left-hand sides of these equations represent the vertical gradient of the mean wind speed, virtual potential temperature, and specific humidity. The terms u' and v' are components of transverse wind velocity fluctuations, while w' is the vertical wind velocity fluctuation. The expression $(\overline{u'w'}^2 + \overline{v'w'}^2)^{1/4}$ is the friction velocity and k is the von Kármán constant. The covariance terms can all be calculated using eddy-covariance techniques based on data collected with the fast-response sensors. Integration of Eqs. (2) yields vertical profiles for the mean quantities, $\overline{q}$, $\overline{\theta_v}$, and $\overline{u_h}$. Both $\overline{q}$ and $\overline{\theta_v}$ relate to the air temperature and water vapor pressure given in Eq. (1) and together with a pressure profile derived from bulk readings and the assumption of hydrostatic equilibrium, a profile of modified refractivity, M, can be calculated. The stability functions adopted for the profile calculations were

$$\phi_m(\zeta) = (1 - 16\zeta)^{-1/4} \text{ and}$$
$$\phi_H(\zeta) = \phi_M(\zeta) = (1 - 16\zeta)^{-1/2},$$

where the parameter ζ is a dimensionless length scale defined by $\zeta = z/L$ and z is height and L is the Obukhov length given by

$$L = \frac{-\overline{\theta_\upsilon}\left(\overline{u'w'}^2 + \overline{\upsilon'w'}^2\right)^{3/4}}{kg\overline{\theta_\upsilon' w'}}. \qquad (3)$$

Various stability functions have been proposed over the years (Battaglia 1985; Musson-Genon et al. 1992; Claverie et al. 1994, 1998; Grachev et al. 2000; Foken 2006), but the choice of these stability functions was motivated by an earlier study (yet unpublished) that showed preference for this form.

On the morning of 26 November, the aircraft data show the remnants of a stable nocturnal layer above 70 m. The inherent limitations of Monin–Obukhov similarity theory preclude this feature from being captured in the flux-derived profile. By early afternoon, the nocturnal layer is no longer present and good agreement is seen between aircraft- and flux-derived refractivity profiles (Fig. 10). This agreement was typical when the atmosphere was absent of mesoscale flows and winds were directed onshore, which was the case throughout the campaign when the variable RF link was operational. Preliminary results from this ongoing analysis of jetty–aircraft refractivity profile comparisons show that there is mostly good agreement between the jetty results and aircraft data when the aircraft is within about 15 km of the jetty. A certain decorrelation between the jetty and aircraft measurements is to be expected as

the aircraft moves away from the jetty, and surface and atmospheric conditions change. When the aircraft was beyond 30 km, there was only occasional agreement between the aircraft profiles and the jetty results.

Kitesonde and PIRAM. Examples of kitesonde data from one descent are shown in Fig. 11. To compare the data with the surface-layer profiles, results from the PIRAM surface-layer model are shown. The PIRAM model relies on integration of the flux–gradient relationships for moisture and temperature with the fluxes parameterized by the iterative scheme based on bulk atmospheric humidity and temperature measurements (Claverie et al. 1994). In this case, the bulk parameters were obtained from the jetty tower data. The PIRAM model uses an appropriate stability function to account for the thermally unstable surface layer and compares well with the data (Claverie et al. 1998).

RF propagation. The signal path loss can be modeled by multiplying the free-space loss by a propagation factor F^2, which takes into account diffraction, refraction, multipath reflection effects, and signal attenuations due to atmospheric constituents. The modeled path loss is defined as the propagation factor multiplied by the free-space loss:

$$L_{\text{path}} = L_{\text{freespace}} F^2 = \left(\frac{\lambda}{4\pi R}\right)^2 F^2. \qquad (4)$$

In this equation, λ is the carrier frequency wavelength and R is the distance from the transmitter.

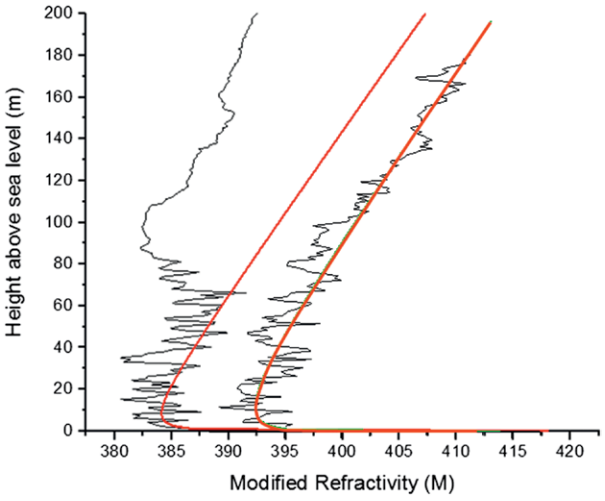

Fig. 10. Vertical distribution of modified refractivity *M* on 26 Nov 2013 computed from ECO-Dimona measurements (black) and modeled by Monin–Obukhov similarity theory using fluxes from the jetty (red). The aircraft was (left) near the jetty in the morning and (right) about 6 km away from the jetty in the early afternoon.

The propagation path losses for the three RF links associated with one 35-GHz source at Lucinda and the three-receiver element network on the R/V on 5 December 2013 are shown as the solid curves in Fig. 12. The curves were derived from 125-MHz-sampled, 15-ms-power spectral estimates of the characteristic waveform signal demodulated from the transmissions. A 51-point smoothing filters the fast-fading data effects typical of RF link measurement (Saunders 2003). Figure 12 also shows a single-path loss curve modeled for the case of a standard atmosphere (dashed curve). A "standard atmosphere" is defined by a linear increase in modified refractivity with height, $M = 0.118z$ (m^{-1}), where z is the height (m) (COESA 1976). Because the vertical slope of the modified refractivity for a standard atmosphere is positive, ducting of RF energy does not occur and path losses increase at a far greater rate than those measured by the 35-GHz link for ranges greater than 14 km, which is

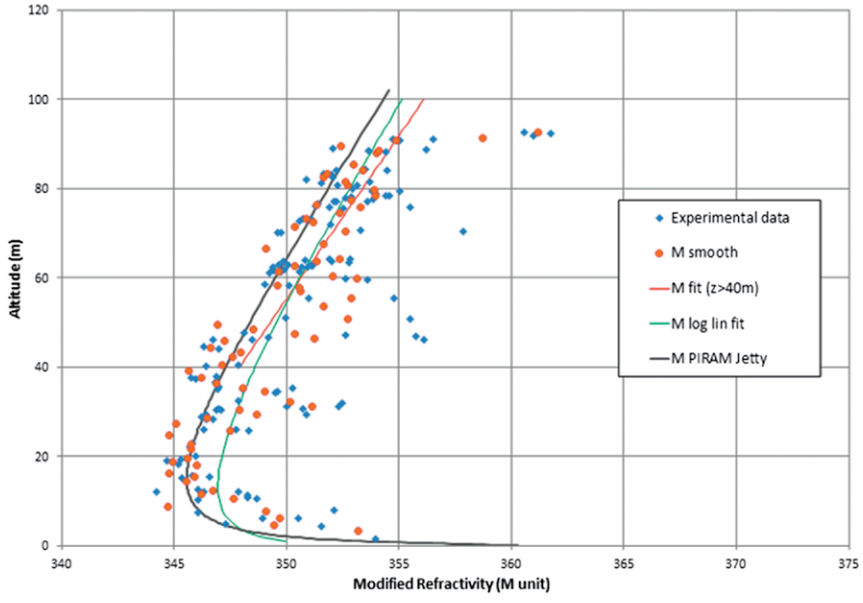

Fig. 11. Examples of kitesonde data (blue diamonds) from one descent measured on 3 Dec 2013. The red dots are smoothed kitesonde results. The gray curve is the evaporation duct as modeled by PIRAM using bulk jetty data.

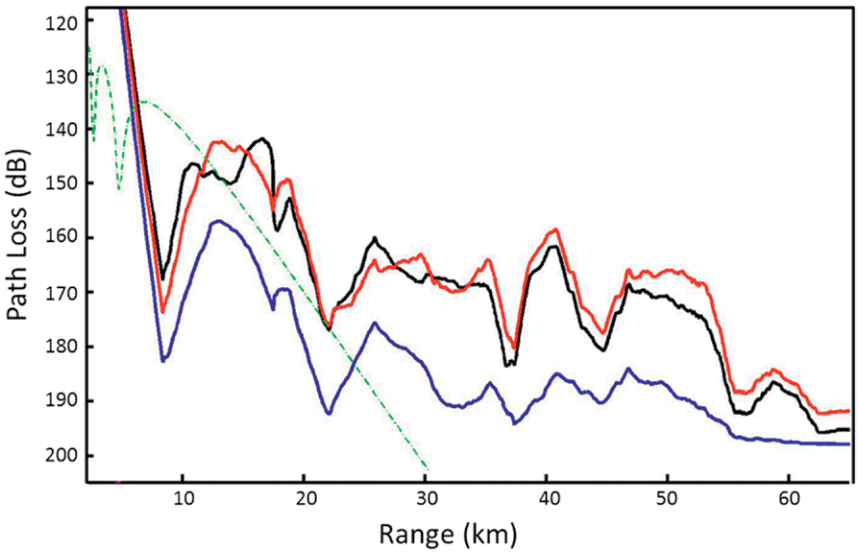

Fig. 12. The absolute value of measured path losses at three heights—3.4 (blue), 8.7 (red), and 11.3 m (black)—on 5 Dec 2013 from 35-GHz transmission at a height of 3.5 m along the Lucinda shore. Modeled losses are shown for a standard atmosphere (green dashed).

considered beyond the line of sight for the geometry of the transmit and receive antennas. This result is best explained by the presence of evaporation ducting, which enhances signal power over the horizon.

The effects of ducting are also shown in Fig. 13, which plots the calibrated received power from a vessel of opportunity transiting along a north–south shipping lane on 5 December. The vessel can be seen far beyond the radio horizon, which is approximately 31 km for this geometry, indicating the presence of surface-layer ducting. For all days of the study the observed path loss was less than the model prediction for a standard atmosphere, indicating the presence of a duct at the surface. From the evolution of evaporation duct heights (Fig. 8), daytime heights were typically above 12 m, suggesting that the sensors were operating within the surface-layer evaporation duct. As an interesting comparison, Fig. 13 also shows the "free space" power-loss curve, that is, the loss due to the $(\lambda/4\pi R)^2$ term in Eq. (4). Out to a range of 60 km, sufficient energy is trapped by the duct so that the only apparent signal loss is that due to the free-space term.

Troposcatter effects on digital television transmissions are shown in Fig. 14 for the Ingham-to-Townsville link (T_2 in Fig. 4). A time series of power measurements, referenced to the mean power, is shown against predictions calculated by inputting radiosondes from Ingham into the Advanced Propagation Model (APM; Patterson 2008). Although the distance between Ingham and the transmitter at Townsville results in a small signal variation, there is a discernible correlation between the observed meteorology and the observed signals. Future comparisons include comparing estimates of c_n^2 estimated from in situ observations and NWP model output with observed signal characteristics.

SUMMARY AND OUTLOOK. The TAPS campaign has provided researchers with an extensive and unique dataset for clear-air tropical littoral conditions around Australia's Great Barrier Reef that includes surface-layer turbulence fluxes, bulk parameters, and profiles within the surface layer and marine atmospheric boundary layer, together with a valuable RF dataset extending from UHF to EHF bands. Additionally, model representations of the environment from four high-resolution NWP forecasts covering the 12-day experiment from 24 November to 5 December 2013 were archived. The comprehensive and coordinated atmospheric and RF measurements allow for validation of the RF coverage forecasting methodologies based on the use of NWP and surface-layer models, as well as hybrid propagation models.

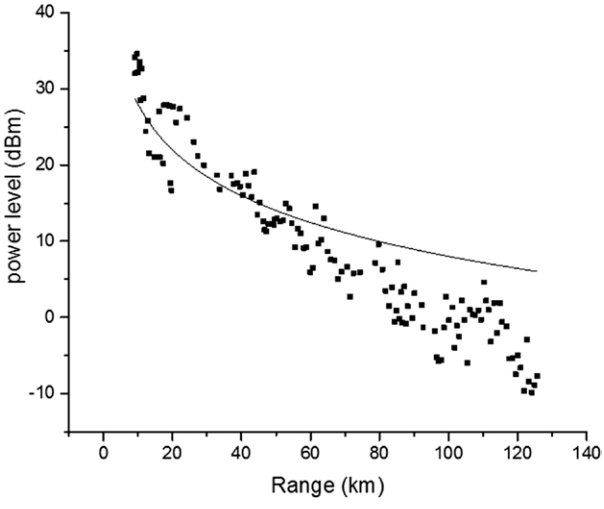

Fig. 13. The received power level (dB*m*, dotted curve) as measured by the TeKI receiver on board the R/V *Cape Ferguson*, on 5 Dec 2013, from a transiting ship navigation radar operating at 9.4 GHz. The solid curve represents the modeled free-space received power level.

During the TAPS campaign, surface wind speeds were somewhat less than expected for the time of year and as a result evaporation ducts were smaller. There was evidence of sea-breeze circulations producing an elevated duct structure. Surface ducts due to the remnants of nocturnal inversions were also observed closer to the coastline. A capping inversion above the marine atmospheric boundary layer also produced a strong elevated duct.

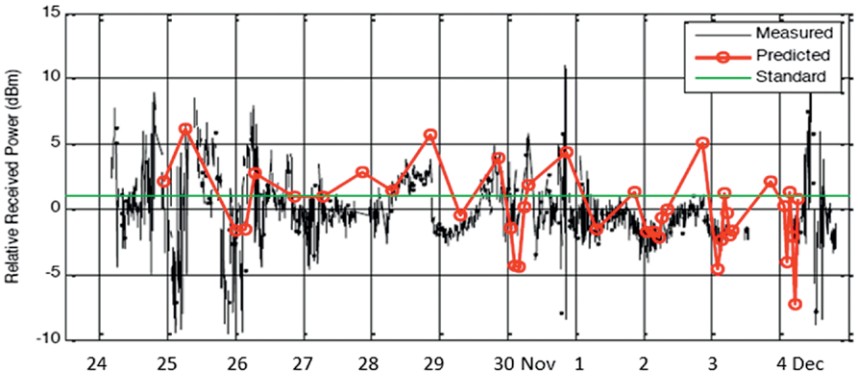

Fig. 14. Time series of variations of observed (black) and model-predicted (red) received power (dB*m*) relative to the respective mean values received in Ingham from the 599.5-MHz carrier-frequency-transmitting antenna in Townsville. For reference, the relative received power for a standard atmosphere is also shown (green).

First results comparing refractivity measurements from the aircraft and kitesonde data against profiles derived from Monin–Obukhov similarity theory using stability functions consistent with the tropical TAPS environment show good agreement in the absence of nocturnal stable layers and when the prevailing winds were onshore. The SHF and EHF RF measurements presented here show evidence of extended (beyond the line of sight) propagation, most likely due to evaporation ducting. Beyond-the-line-of-sight ranges for the UHF emissions were due to troposcatter. Preliminary results from the NWP modeling show that there are differences between model predictions of elevated duct structure and measurements.

Currently, there are several elements of ongoing research and analysis originating from the TAPS field campaign. These are summarized below:

i) investigation of the detailed structure of the surface layer and marine boundary layer refractivity, extending down to the surface, from the aircraft, kitesonde, radiosonde, and jetty instrumented tower data;
ii) a comparison of blended profiles of surface-layer models and NWP model results with actual measurements; the focus is on how accurately each model forecasts the elevated ducting, surface ducting, superrefractive structure, and evaporation ducting that was observed during the campaign;
iii) improvements to the NWP modeling systems used by each country to improve surface and marine boundary layer characterization and the prediction of refractive structures;
iv) investigation of heat, buoyancy, moisture, and momentum fluxes in coastal regions, including inland and over water;
v) investigation of heat, buoyancy, moisture, and momentum fluxes over the sea, including over coral lagoons in the Great Barrier Reef;
vi) comparison of various propagation model outputs with measured RF data; it is anticipated that propagation models may need to be improved for the accurate prediction of EHF (millimeter wave) propagation in superrefractive and ducting environments, as propagation at these frequencies is sensitive to sea states, wind waves, and roughness; and
vii) investigation of troposcatter results and models for UHF signals. Improved troposcatter prediction is required, especially for UHF signals. It should also be pointed out that the use of signals of opportunity to remotely sense refractivity information have been made possible by the successful TAPS meteorological and RF measurement and modeling campaign.

These analysis activities are directly relevant to the primary focus of the TAPS campaign, that is, the investigation of a methodology for forecasting RF coverage and to validate the end-to-end propagation forecasting process by enabling comparisons between observed and modeled meteorology and collocated observed and modeled RF coverage.

ACKNOWLEDGMENTS. We acknowledge Queensland Sugar Limited, Inline Technologies Pty., Ltd., James Cook University, Australian Institute of Marine Science, North Queensland Aviation Services, and the Australian

Bureau of Meteorology for logistical and technical support, prior to and throughout the TAPS campaign. We are grateful to DSTO for organizing and managing the TAPS campaign and especially thank Dr. Warren Marwood (DSTO).

REFERENCES

Anderson, K. B., and Coauthors, 2004: The RED Experiment: An assessment of boundary layer effects in a trade winds regime on microwave and infrared propagation over the sea. *Bull. Amer. Meteor. Soc.*, **85**, 1355–1365, doi:10.1175/BAMS-85-9-1355.

Atkinson, B. W., and M. Zhu, 2006: Coastal effects on radar propagation in atmospheric ducting conditions. *Meteor. Appl.*, **13**, 53–62, doi:10.1017/S1350482705001970.

Barrios, A. E., 1992: Parabolic equation modeling in horizontally inhomogeneous environments. *IEEE Trans. Antennas Propag.*, **40**, 791–797, doi:10.1109/8.155744.

Battaglia, M. R., 1985: Modelling the radar evaporative duct. RANRL Tech. Note 3/85, 43 pp. [Available online at www.dtic.mil/dtic/tr/fulltext/u2/a161542.pdf.]

Bradley, E. F., 2003: Observational techniques. *Encyclopedia of Atmospheric Sciences*, J. R. Holton, J. Pyle, and J. A. Curry, Eds., Academic Press, 280–290.

Brooks, I. M., A. K. Goroch, and D. P. Rogers, 1999: Observations of strong surface radar ducts over the Persian Gulf. *J. Appl. Meteor.*, **38**, 1293–1310, doi:10.1175/1520-0450(1999)038<1293:OOSSRD>2.0.CO;2.

Brown, A., S. Milton, M. Cullen, B. Golding, J. Mitchell, and A. Shelly, 2012: Unified modeling and prediction of weather and climate: A 25-year journey. *Bull. Amer. Meteor. Soc.*, **93**, 1865–1877, doi:10.1175/BAMS-D-12-00018.1.

Burba, G., and D. Anderson, 2012: *A Brief Practical Guide to Eddy Covariance Flux Measurements: Principles and Workflow Examples for Scientific and Industrial Applications*. Li-Cor Biosciences. 212 pp.

Burk, S. D., T. Haack, L. T. Rogers, and L. J. Wagner, 2003: Island wake dynamics and wake influence on evaporation duct and radar propagation. *J. Appl. Meteor.*, **42**, 349–367, doi:10.1175/1520-0450(2003)042<0349:IWDAWI>2.0.CO;2.

Burrows, W. G., 1968: *VHF Radiowave Propagation in the Troposphere*. Intertext, 130 pp.

Claverie, J., and Y. Hurtaud, 1992: Propagation transhorizon en atmosphère marine—Modélisation et nouveaux résultats expérimentaux. *Remote Sensing of the Propagation Environment: Papers Presented at the Electromagnetic Wave Propagation Panel Symposium*, Advisory Group for Aerospace Research and Development Conf. Publ. AGARD-CP-502, 4.1–4.14.

——, ——, Y. De Fromont, and A. Junchat, 1994: Modelisations profils verticaux d'indice de refraction et de c_n^2 en atmosphere marine. *Propagation Assessment in Coastal Environments*, Advisory Group for Aerospace Research and Development Conf. Publ. AGARD-CP-567, 29.1–29.9.

——, B. Tranchant, P. Mestayer, A. M. J. Van Eijk, and Y. Hurtaud, 1998: Effets de la refraction atmospherique sur la propagation infrarouge dans la basse atmosphere marine–comparaison des modeles SEACLUSE et PIRAM. *Proc. Symp. on E-O Propagation, Signature and System Performance under Adverse Meteorological Conditions Considering Out-of-Area Operations*, Naples, Italy, NATO RTO, 5.1–5.12.

COESA, 1976: U.*S. Standard Atmosphere, 1976*. NOAA, 227 pp. [Available online at http://ntrs.nasa.gov/archive/nasa/casi.ntrs.nasa.gov/19770009539.pdf.]

Craig, K. H., and M. F. Levy, 1991: Parabolic equation modelling of the effects of multipath and ducting on radar systems. *IEE Proc.*, **138F**, 153–162, 10.1049/ip-f-2.1991.0021.

Dockery, G. D., and J. R. Kuttler, 1996: An improved impedance-boundary algorithm for Fourier split-step solutions of the parabolic wave equation. *IEEE Trans. Antennas Propag.*, **44**, 1592–1599, doi:10.1109/8.546245.

Essen, H., H.-H. Fuchs, and A. Pagels, 2006: Radar propagation in coastal environments: VAMPIRA results. *Optics in Atmospheric Propagation and Adaptive Systems IX*, A. Kohnle and K. Stein, Eds., International Society for Optical Engineering (SPIE Proceedings, Vol. 6364), 636408-1–636408-8, doi:10.1117/12.693498.

Foken, T., 2006: 50 years of the Monin–Obukhov similarity theory. *Bound.-Layer Meteor.*, **119**, 431–447, doi:10.1007/s10546-006-9048-6.

Garratt, J. R., 1994: *The Atmospheric Boundary Layer*. Cambridge University Press, 316 pp.

Garrett, S. A., D. E. Cook, and R. E. Marshall, 2009: The Sea Breeze 2009 Experiment: Investigating the impact of ocean and atmospheric processes on radio performance in the Bay of Plenty, New Zealand. *Wea. Climate*, **31**, 82–100.

Grachev, A. A., C. W. Fairall, and E. F. Bradley, 2000: Convective profile constants revisited. *Bound.-Layer Meteor.*, **94**, 495–515, doi:10.1023/A:1002452529672.

Haack, T., and S. D. Burk, 2001: Summertime marine refractivity conditions along coastal California. *J. Appl. Meteor.*, **40**, 673–687, doi:10.1175/1520-0450(2001)040<0673:SMRCAC>2.0.CO;2.

——, C. Wang, S. Garrett, A. Glazer, J. Mailhot, and R. Marshall, 2010: Mesoscale modeling of boundary layer refractivity and atmospheric ducting. *J. Appl. Meteor. Climatol.*, **49**, 2437–2457, doi:10.1175/2010JAMC2415.1.

Harish, A. R., and M. Sachidananda, 2007: *Antennas and Wave Propagation*. Oxford University Press, 402 pp.

Hodur, R. M., 1997: The Naval Research Laboratory's Coupled Ocean/Atmosphere Mesoscale Prediction System (COAMPS). *Mon. Wea. Rev.*, **125**, 1414–1430, doi:10.1175/1520-0493(1997)125<1414:TNRLSC>2.0.CO;2.

Holm, P. D., 2007: Wide angle shift-map PE for a piecewise linear terrain—A finite-difference approach. *IEEE Trans. Antennas Propag.*, **55**, 2773–2789, doi:10.1109/TAP.2007.905865.

Hurtaud, Y., and J. Claverie, 2015: Geophysical information inputs for computing the performance of EM systems in littoral environments. *Radio Sci. Bull.*, **353**, 10–16.

——, ——, E. Mandine, and M. Aidonidis, 2008: Une préfiguration des futures aides tactiques: le code PREDEM. *Rev. Electr. Electron.,* 31–41.

Karimian, A., C. Yardim, T. Haack, P. Gerstoft, W. S. Hodgkiss, and T. Rogers, 2013: Toward the assimilation of the atmospheric surface layer using numerical weather prediction and radar clutter observations. *J. Appl. Meteor. Climatol.*, **52**, 2345–2355, doi:10.1175/JAMC-D-12-0320.1.

Kerans, A. J., and G. S. Woods, 2004: Observations of anomalous over the horizon microwave radio propagation inside the tropical maritime evaporation duct in North Queensland, Australia. Part One: Normal ducting events. *Proceedings of URSI Commission F Triennium Open Symposium 2004,* URSI Commission F.

——, A. S. Kulessa, J. Hermann, and G. S. Woods, 2000: Evaporation duct statistics around Australia and the West Pacific. *Proc. AP2000 Millenium Conf. on Antennas and Propagation*, Davos, Switzerland, European Space Agency.

Kulessa, A. S., and J. M. Hacker, 2010: Determining the refractive index structure in the littoral marine boundary layer by *in situ* measurements and sensing techniques. *2010 International Conference on Electromagnetics in Advanced Applications*, IEEE, 172–175, doi:10.1109/ICEAA.2010.5652999.

——, M. L. Heron, and G. S. Woods, 1997: Temporal variations in evaporation duct heights. *Proc. Workshop on the Applications of Radio Science*, Leura, NSW, Australia, National Committee for Radio Science, Australian Academy of Science, 165–170.

——, G. S. Woods, B. Piper, and M. L. Heron, 1998: Line-of-sight EM propagation experiment at 10.25 GHz in the tropical ocean evaporation duct. *IEE Proc.*, **145H**, 65–69, doi:10.1049/ip-map:19981474.

Lee, X., W. J. Massman, and B. Law, 2008: *Handbook of Micrometeorology: A Guide for Surface Flux Measurement and Analysis*. Kluwer, 250 pp.

Levy, M. F., 2000: *Parabolic Equation Methods for Electromagnetic Wave Propagation*. Electromagnetic Waves Series, Vol. 45, IEE, 336 pp.

Lowry, A. R., C. Rocken, S. V. Sokolovskiy, and K. D. Anderson, 2002: Vertical profiling of atmospheric refractivity from ground-based GPS. *Radio Sci.*, **37**, 1041–1060, doi:10.1029/2000RS002565.

Marshall, R. E., and K. L. Horgan, 2011: Multi-wavelength radar target detection in an extreme advection duct event. *Int. J. Microwave Wireless Technol.*, **3**, 373–381, doi:10.1017/S1759078711000225.

Monin, A. S., and A. M. Obukhov, 1954: Basic turbulent mixing laws in the atmospheric surface layer. *Tr. Geofiz. Inst., Akad. Nauk SSSR*, **24**, 163–187.

Musson-Genon, L., S. Gauthier, and E. Bruth, 1992: A simple method to determine evaporation duct height in the sea surface boundary layer. *Radio Sci.*, **27**, 635–644, doi:10.1029/92RS00926.

Nilsson, T., and R. Haas, 2010: Impact of atmospheric turbulence on geodetic very long baseline interferometry. *J. Geophys. Res.*, **115**, B03407, doi:10.1029/2009JB006579.

Page, G., S. Bainbridge, and S. Gardner, 2014: Implementation of low-cost, long range microwave links on the Great Barrier Reef using evaporation duct transmission. *Proc. IEEE Oceans Conf. Taipei*, Taipei, Taiwan, IEEE, 4 pp., doi:10.1109/OCEANS-TAIPEI.2014.6964340.

Patterson, W., 2008: The propagation factor, Fp, in the radar equation. *The Radar Handbook*, M. Skolnik, Ed., 3rd ed. McGraw Hill, 26.1–26.28.

Paulus, R. A., 1994: VOCAR: An experiment in variability of coastal atmospheric refractivity. *IGARSS'94: International Geoscience and Remote Symposium; Surface and Atmospheric Sensing: Technologies, Data Analysis and Interpretation*, Vol. 1, IEEE, 386–388, doi:10.1109/IGARSS.1994.399132.

Pielke, R. A., and Coauthors, 1992: A comprehensive meteorological modeling system—RAMS. *Meteor. Atmos. Phys.*, **49**, 69–91, doi:10.1007/BF01025401.

Rogers, L. T., 1996: Remote sensing of evaporation ducts using SHF propagation measurements. *Remote Sensing: A Valuable Source of Information*, AGARD Conference Series 582, Advisory Group for Aerospace Research and Development Conf. Publ. AGARD-CP-582, 7.1–7.13.

——, C. P. Hattan, and J. K. Stapleton, 2000: Estimating evaporation duct heights from radar sea echo. *Radio Sci.*, **35**, 955–966, doi:10.1029/1999RS002275.

Saunders, S. R., 2003: Outdoor mobile propagation. *Propagation of Radiowaves*, 2nd ed. L. W. Barclay, Ed., Electromagnetic Wave Series, Vol. 502, Institution of Engineering and Technology, 185–222.

Schotanus, P., F. T. M. Niewstadt, and H. A. R. de Bruin, 1983: Temperature measurement with a sonic anemometer and its applications to heat and moisture fluxes. *Bound.-Layer Meteor.*, **26**, 81–93, doi:10.1007/BF00164332.

Seity, Y., P. Brousseau, S. Malardel, G. Hello, P. Bénard, F. Bouttier, C. Lac, and V. Masson, 2011: The AROME-France convective scale operational model. *Mon. Wea. Rev.*, **139**, 976–991, doi:10.1175/2010MWR3425.1.

Silveira, R. B., and O. Massambani, 1995: The effects of atmospheric circulation on line-of-sight microwave links. *Radio Sci.*, **30**, 1447–1458, doi:10.1029/95RS01355.

Stapleton, J., D. Shanklin, V. Wiss, T. Nguyen, and E. Burgess, 2001: Radar propagation modeling assessment using measured refractivity and directly sensed propagation ground truth. Naval Surface Warfare Center Dahlgren Division Tech. Rep. NSWCDD/TR-01/132, 49 pp.

Thompson, W. T., and T. Haack, 2011: An investigation of sea surface temperature influence on microwave refractivity: The Wallops-2000 Experiment. *J. Appl. Meteor. Climatol.*, **50**, 2319–2337, doi:10.1175/JAMC-D-10-05002.1.

Wang, C., D. Wilson, T. Haack, P. Clark, H. Lean, and R. Marshall, 2012: Effects of initial and boundary conditions of mesoscale models on simulated atmospheric refractivity. *J. Appl. Meteor. Climatol.*, **51**, 115–131, doi:10.1175/JAMC-D-11-012.1.

Woods, G. S., C. M. Palazzi, A. Kulessa, and D. L. Maskell, 2006: ReefGrid–A communications network on the Great Barrier Reef. *Proc. Oceans 2006 Asia-Pacific Conf.*, Singapore, IEEE, 6 pp., doi:10.1109/OCEANSAP.2006.4393850.

——, A. Ruxton, C. Huddlestone-Holmes, and G. Gigan, 2009: High-capacity, long-range, over ocean, microwave link using the evaporation duct. *IEEE Oceanic Eng.*, **34**, 323–330, doi:10.1109/JOE.2009.2020851.

Xiaofeng, Z., and H. Sixun, 2012: Estimation of atmospheric duct structure using radar sea clutter. *J. Atmos. Sci.*, **69**, 2808–2818, doi:10.1175/JAS-D-12-073.1.

Yardim, C., 2007: Statistical estimation and tracking of refractivity from radar clutter. Ph.D. dissertation, University of California, San Diego, 136 pp. [Available online at http://escholarship.org/uc/item/3xn5116w.]

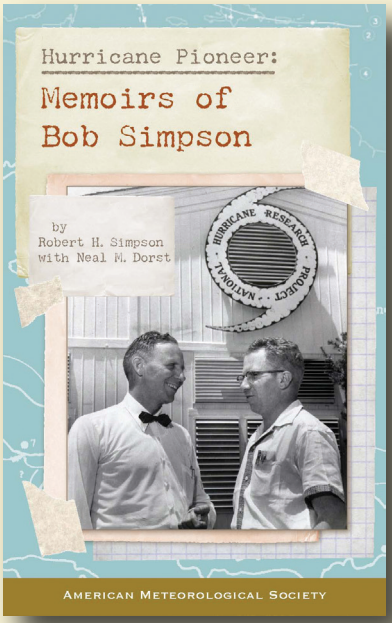

HURRICANE PIONEER

Memoirs of Bob Simpson

Robert H. Simpson with Neal M. Dorst

In 1951, Bob Simpson rode a plane directly into the wall of a hurricane—just one of his many pioneering explorations. This autobiography of the first director of the National Hurricane Research Project and co-creator of the Saffir-Simpson Hurricane Scale starts with childhood remem-mbrance and ends in first-hand account of a revolutionary

© 2014, PAPERBACK
ISBN: 978-1-935704-75-1
LIST $30 MEMBER $20

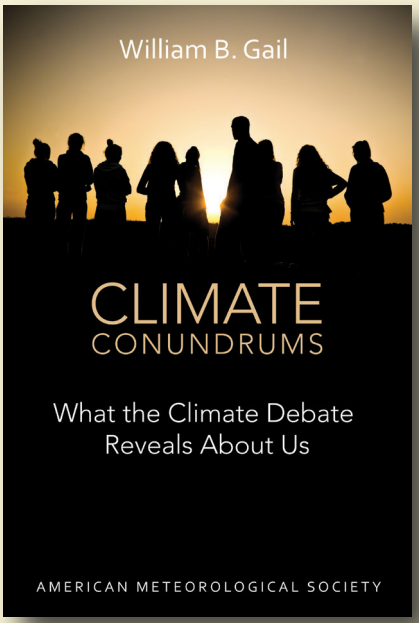

CLIMATE CONUNDRUMS

What the Climate Debate Reveals About Us

William B. Gail

This is a journey through how we think, individually and collectively, derived from the climate change debate. With wit and wisdom, Gail explores several questions: Can we make nature better? Could science and religion reconcile? Insights from such issues can help us better understand who we are and help

© 2014, PAPERBACK
ISBN: 978-1-935704-74-4
LIST $30 MEMBER $20

Browse online at
ametsoc.org/bookstore

FREE SHIPPING
for AMS Members!

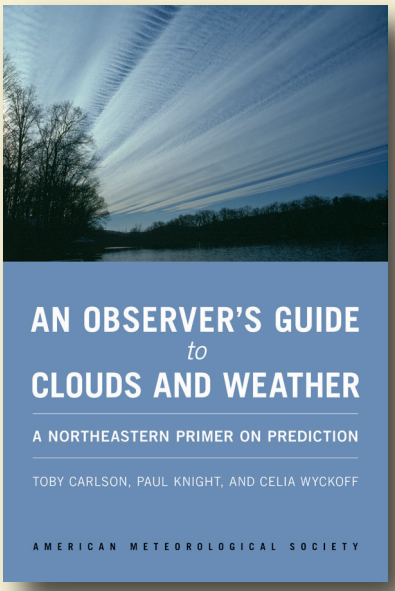

AN OBSERVER'S GUIDE TO CLOUDS AND WEATHER

A Northeast Primer on Prediction

Toby Carlson, Paul Knight, and Celia Wyckoff

With help from Penn State experts, start at the beginning and go deep. This primer for enthusiasts and new students alike will leave you with both refined observation skills and an understanding of the complex science behind the weather: the ingredients for making reliable predictions of your own.

© 2014, PAPERBACK
ISBN: 978-1-935704-58-4
LIST $35 MEMBER $20

AMS BOOKS

AMS Books are available to groups and booksellers, and desk copies may be obtained, through our distributor The University of Chicago Press: 1-800-621-2736 or custserv@press.uchicago.edu.